Chapter 5

The distribution of stellar mass in galaxy clusters at $z \sim 0.15$

We study the radial galaxy and stellar mass density distributions in a sample of 10 galaxy clusters at $0.07 < z < 0.26$ selected from two surveys; the Multi-Epoch Nearby Cluster Survey (MENeaCS) and the Canadian Cluster Comparison Project (CCCP). Deep *ugri*-band imaging is used to estimate photometric redshifts and stellar masses, and then statistically subtract fore-, and background sources using data from the COSMOS survey. This procedure performs well, given that identical results are obtained for the ensemble cluster by considering the ~ 3000 spectroscopically confirmed member galaxies which make up the bulk of the stellar mass. We find that the radial distribution of stellar mass is well-described by an NFW distribution with concentrations in the range $0.8 < c < 5.6$, and an ensemble averaged value of $c = 1.92 \pm 0.19$ (1-σ statistical). We estimate an intrinsic scatter of $\sigma_{c,\mathrm{int}} = 0.70^{+0.33}_{-0.22}$ (or $\sigma_{\log_{10}c,\mathrm{int}} = 0.25 \pm 0.05$ dex), which is likely caused by a combination of centroiding uncertainties, a range of different halo assembly histories, and different orientations on the sky.

The halo masses, which range from $4.8 \times 10^{14}\mathrm{M}_{\odot}$ to $2.3 \times 10^{15}\mathrm{M}_{\odot}$ (M_{200c}), match the approximate descendent population of the GCLASS cluster sample at $z \sim 1$, for which a stellar mass concentration of $c = 7.12^{+1.53}_{-0.99}$ was estimated. A comparison of these results shows that the spatial distribution of stellar mass evolves substantially towards low-z, a trend that is opposite to what is found for the dark-matter distribution in N-body simulations. We compare the stellar mass density distributions at $z \sim 1$ and $z \sim 0.15$ in the same physical units, showing that the stellar mass density in the cluster cores (R<0.2 Mpc) decreases since $z \sim 1$. This may be related to the build-up of the ICL+BCG component over cosmic time. We also find that the clusters at $z \sim 1$ have

to grow in stellar mass at larger radii to match the descendent population. Comparisons with simulations have the potential to provide constraints on the stellar mass content of haloes falling into these clusters, and the dynamical friction time-scale that is applied in semi-analytic models.

Remco F.J. van der Burg, Henk Hoekstra, Adam Muzzin, Cristóbal Sifón, Sean McGee, Michael Balogh
In preparation

5.1 Introduction

A key open question in the field of extragalactic astronomy today is to understand how galaxies form in our dark-matter dominated Universe (e.g. Guo et al. 2010). To learn about the baryonic physics that govern complex processes such as the cooling of gas, formation of stars and several feedback modes, models need to be tailored to match the observations. Observational probes such as the luminosity function and stellar mass function (e.g. Bell et al. 2003; Pérez-González et al. 2008; Ilbert et al. 2010; Muzzin et al. 2013a) have been used as fundamental observables to constrain physical models (e.g. Henriques et al. 2012; Weinmann et al. 2012), or test results from hydrodynamical simulations (e.g. Schaye et al. 2010; Cen 2014). Galaxies are not randomly distributed in space, and properties such as the star-formation rate (SFR), morphology, stellar mass, and metallicity of galaxies are dependent on their environment (Dressler 1980; Kauffmann et al. 2004; Baldry et al. 2006; Muzzin et al. 2012; Woo et al. 2013; van der Burg et al. 2013). Central galaxies and satellite galaxies, the latter of which are typically lower mass galaxies that are part of the same halo, evolve in different ways and are thus studied separately (Peng et al. 2010, 2012; Knobel et al. 2013).

The observed abundance and spatial distribution of satellite galaxies provide further constraints on galaxy formation models. A comparison between the outcomes of numerical N-body simulations and observations has revealed a problem known as the 'missing satellites problem' (Klypin et al. 1999; Bullock 2010). The amount of satellite galaxies in the local group is significantly lower than predicted by the ΛCDM model. A possible interpretation of this is the inefficiently of low-mass haloes in forming stars, possibly due to supernova feedback (Efstathiou 2000; Dalla Vecchia & Schaye 2008), stellar winds, and the presence of a photo-ionizing background (Benson et al. 2002). It may also hint at a fundamental problem with our fiducial ΛCDM model, such that simulated haloes have more substructure (i.e. sub-haloes) than haloes in the actual Universe (Boylan-Kolchin et al. 2011).

Given the (nearly) self-similar properties of dark matter haloes, we can test the ΛCDM model by studying more massive haloes such as galaxy groups and clusters. Sub-haloes in these systems are correspondingly more massive, which makes them more efficient at forming stars, and thus easier to identify through observations. However, on the theory side this comparison also has limitations. Most studies are based on large N-body simulations (Springel et al. 2005), and dark matter haloes falling into larger haloes experience tidal forces leading to the stripping of their constituent particles (Ghigna et al. 2000; Binney & Tremaine 2008), also see Natarajan et al. (2002); Gillis et al. (2013) for an observational study. As a sub-halo falls into the main halo, it will continuously lose mass through the process of tidal stripping, and it may eventually fall below the mass resolution of the simulation. The sub-halo is

then no longer identified as such, its mass is deposited on the central galaxy or dispersed between the galaxies, and its orbit is no longer defined. For this reason, the radial distribution of sub-haloes is less concentrated than the dark matter in N-body simulations (Nagai & Kravtsov 2005). While the sub-haloes in these dissipationless simulations are eventually destroyed, the galaxies that have formed inside of them are expected to be more resistive to tidal forces. In semi-analytic models of galaxy formation, which are based on merger trees from these simulations, the more concentrated baryonic parts of galaxies are followed analytically after the sub-halo is dispersed (Bower et al. 2006; De Lucia & Blaizot 2007). A dynamical friction time-scale is generally applied, which determines when the galaxy is deposited onto the central galaxy, and how the intra-cluster light is building up (Contini et al. 2013). Measurements of the growth of brightest cluster galaxies (BCGs) (Lin & Mohr 2004; Lidman et al. 2012, 2013) and the intracluster light (ICL) (Gonzalez et al. 2013) can be used to constrain this time-scale, as the build-up of these components are directly related to the in-fall of satellite galaxies.

The radial number and stellar mass density distribution of satellite galaxies directly probe the abundance of sub-haloes, and can also be used to constrain the dynamical friction time-scale. These distributions are observed to be well described by NFW (Navarro et al. 1997) profiles for group-sized haloes and clusters from the local Universe to $z \sim 1$ (Carlberg et al. 1997; Lin et al. 2004; Muzzin et al. 2007; Giodini et al. 2009; Budzynski et al. 2012; van der Burg et al. 2014). Each observational study however is based on a different data set and analysis, and presents results in a different form. Lin et al. (2004) and Budzynski et al. (2012) study the number density of galaxies, but due to mergers and interactions between galaxies, the number density distribution of galaxies can be different for galaxies with different luminosities or stellar masses. Their results are therefore dependent on the depth of their data set. Giodini et al. (2009) measure the number density distribution of generally lower mass systems from the COSMOS field. Carlberg et al. (1997) and Muzzin et al. (2007) measure the luminosity density distribution in the r-band and K-band, respectively, for the CNOC1 (Yee et al. 1996) cluster sample. The advantage of this measurement is that, provided the measurements extend significantly below the characteristic luminosity L^*, it is almost insensitive to the precise luminosity cut. That is because the total luminosity in each radial bin is dominated by galaxies around L^*. However, especially in the r-band it is not straightforward to relate the luminosity distribution to a stellar mass distribution due to differences in mass-to-light-ratio between different galaxy types, and because the distributions of these types vary spatially. Inconsistencies between all these studies prevent us from drawing firm conclusions on comparisons between them.

The number density (down to galaxies with stellar mass $10^{10.2}\,\mathrm{M}_\odot$) and stellar mass density distribution of galaxies in the GCLASS cluster sample at

$z \sim 1$ have been measured by van der Burg et al. (2014, hereafter vdB14). They find that both distributions are significantly more concentrated than the simulated distribution of dark matter in N-body simulations, and also more concentrated than a stacked weak-lensing measurement of $z \sim 1$ clusters (Sereno & Covone 2013). The only local measurement this study could compare to is the K-band luminosity distribution measured by Muzzin et al. (2007) for the CNOC1 clusters, which are approximate descendants of the GCLASS cluster by halo mass (estimated given the evolution of haloes in N-body simulations). Also the K-band luminosity is a good probe of the stellar mass of galaxies (Bell & de Jong 2001), especially in the local Universe where the clusters are dominated by galaxies with old stellar populations. The comparison suggests that the stellar mass density distribution evolves significantly since $z \sim 1$, and that the distribution becomes less concentrated over cosmic time.

In this paper we present a measurement of the radial galaxy number density and stellar mass density from a sample of approximate descendants of the GCLASS sample, but at a lower redshift of $0.07 < z < 0.26$. We measure these in a way that is as consistent as possible with the GCLASS measurement. In the discussion presented in vdB14 we suggest that the growth of the ICL or the accretion of galaxies onto the outskirts of the cluster could explain the significant evolution between the measurements in GCLASS and CNOC1. In this paper we revisit this discussion by also including the new measurements at $z \sim 0.15$.

The structure of this paper is as follows. In Sect. 5.2 we give an overview of the cluster sample, the available spectroscopic data set and the photometric catalogues based on *ugri*-band photometry. Section 5.3 presents the measurement of the radial density profiles, based on two independent analyses that we will compare for robustness tests. The results are presented in Sect. 5.4, and put into context against low-z literature measurements. In Sect. 5.5 we discuss the observed evolution and suggest possible scenarios to explain the differences between $z \sim 1$ and the local study. We summarise and conclude in Sect. 5.6.

All magnitudes we quote are in the AB magnitudes system (unless explicitly mentioned otherwise) and we adopt ΛCDM cosmology with $\Omega_{\rm m} = 0.3$, $\Omega_\Lambda = 0.7$ and $\rm H_0 = 70\,km\,s^{-1}\,Mpc^{-1}$. For stellar mass estimates we assume the Initial Mass Function (IMF) from Chabrier (2003).

5.2 Data overview & processing

The sample we study is drawn from two large X-ray selected cluster surveys, the Multi-Epoch Nearby Cluster Survey (MENeaCS) and the Canadian Cluster Comparison Project (CCCP). A substantial number of spectroscopic redshifts in these cluster fields are available from the literature, specifically the Cana-

dian Network for Observational Cosmology Survey (CNOC; Yee et al. 1996), the Sloan Digital Sky Survey Data Release 10 (SDSS DR10; Ahn et al. 2013), and the Hectospec Cluster Survey (HeCS; Rines et al. 2013). We searched the NASA/IPAC Extragalactic Database (NED)[1] to obtain additional spectroscopic information for galaxies that have not been targeted by these surveys.

In addition to the determination of cluster membership these redshifts allow us to estimate dynamical masses. We refer to Sifón et al. (in prep.) for details. In summary, cluster membership and velocity dispersions are determined using the standard shifting gapper approach (Fadda et al. 1996), see also Sifón et al. (2013). To relate the velocity dispersion σ_v to estimates of R_{200}, the radius at which the mean interior density is 200 times the critical density ($\rho_{\rm crit}$), and M_{200}, the mass contained within R_{200}, the Evrard et al. (2008) scaling relation is used. See vdB14 (Sect. 2.1) for the application of this scaling relation to the GCLASS cluster sample.

This is a pilot study of 10 clusters which were drawn from those MENeaCS and CCCP clusters that were observed with MegaCam (as opposed to the older CFH12k camera) in the g- and r-bands and have additional u- and i-band photometry to allow for a cleaner cluster galaxy selection. The 10 clusters are listed in Table 5.1, and were selected from the larger sample following several criteria. Firstly, they have high dynamical masses to ensure that they are significantly over-dense compared to the field, which will lead to a clean background subtraction. Secondly, they have a large number of spectroscopic members to test the photometric background subtraction method by only considering the spectroscopically confirmed cluster members. Thirdly, we prioritize fields with low amounts of Galactic dust for a cleaner photometric calibration by exploiting the stellar locus. And finally, in order to not underestimate the concentration of the stellar mass distribution, we exclude known major mergers such as Abell 520 (Mahdavi et al. 2007; Clowe et al. 2012).

Figure 5.1 suggests that this is (within a factor of ~ 2) the mass regime of the likely descendants from GCLASS in the local Universe. Curves in this figure connect haloes selected from the Millennium simulation (Springel et al. 2005) at fixed comoving number density, and are thus approximate growth curves. We also show that the CNOC1 cluster sample, studied by Muzzin et al. (2007), is on this approximate evolutionary sequence, and we will also compare our results to theirs in this paper.

5.2.1 Photometry - MegaCam

Each of these clusters is covered by deep photometric data taken through the g-, and r-filters using MegaCam mounted at the Canada-France-Hawaii Telescope (CFHT), which is a 36 CCD imaging array covering a full 1×1

[1] http://ned.ipac.caltech.edu/

Table 5.1: The 10 Abell clusters selected from MENeaCS and CCCP that form the basis of this study, with their dynamical properties.

Name	$z_{\rm spec}$	RA[a] J2000	DEC[a] J2000	$\sigma_v^{\rm b}$ [km/s]	$M_{200}^{\rm b}$ [10^{14} M$_\odot$]	$R_{200}^{\rm b}$ [Mpc]	Spec-z Total (Members)
A655	0.127	08:25:29.02	47:08:00.10	934 ± 67	8.7 ± 1.9	1.9 ± 0.1	594 (304)
A1033	0.122	10:31:44.31	35:02:28.71	761 ± 85	4.8 ± 1.6	1.5 ± 0.2	496 (171)
A1068	0.139	10:40:44.46	39:57:11.41	1054 ± 138	12.4 ± 4.8	2.1 ± 0.3	621 (134)
A1835	0.252	14:01:02.04	02:52:42.96	1324 ± 104	23.2 ± 5.5	2.5 ± 0.2	690 (273)
A1914	0.167	14:25:56.69	37:49:00.12	962 ± 83	9.4 ± 2.4	1.9 ± 0.2	700 (264)
A2029	0.078	15:10:56.12	05:44:40.81	1103 ± 64	14.6 ± 2.5	2.3 ± 0.1	800 (315)
A2069	0.114	15:24:08.44	29:52:54.59	1026 ± 76	11.6 ± 2.6	2.1 ± 0.2	821 (347)
A2111	0.228	15:39:40.44	34:25:27.48	964 ± 72	9.1 ± 2.0	1.9 ± 0.1	780 (243)
A2142	0.090	15:58:20.08	27:14:01.11	1105 ± 37	14.6 ± 1.5	2.3 ± 0.1	1869 (1061)
A2261	0.226	17:22:27.16	32:07:57.36	976 ± 197	9.5 ± 5.7	1.9 ± 0.4	644 (214)

[a] Coordinates of the BCGs.

[b] Dynamical properties estimated by Sifón et al. (in prep.).

square degree. The data are pre-processed using the *Elixir* pipeline (Magnier & Cuillandre 2004). For MENeaCS, photometric data in the two bands have been taken for these clusters, with a significant dither pattern, and a cadence of several weeks to allow for the detection of type Ia supernovae in these clusters. Data for CCCP have been taken consecutively under the best seeing conditions to facilitate weak-lensing measurements. For the cluster Abell 655 we further retrieved archival MegaCam data in the u-, and i-bands.

The approach we take to process these data further, is largely laid out in van der Burg et al. (2013, hereafter vdB13, Appendix A), and leads to deep image stacks to measure accurate and precise colours for the purpose of estimating photometric redshifts and stellar masses. We homogenise the PSF of each exposure before stacking, as opposed to homogenising the stack. The former approach leads to a final deep image with a cleaner PSF, especially given that the MENeaCS data have been taken under varying conditions and with substantial dithers. The spatially dependent convolution kernel has been chosen such that the PSF in the final stack has the shape of a circular Gaussian. By applying a Gaussian weight function for aperture fluxes we then optimise colour measurements in terms of S/N (see vdB13 (Appendix A); Kuijken 2008).

Given the large number and the range in image quality of the (2 minute deep) MegaCam exposures for the MENeaCS clusters, we stack only the 20 exposures with the best image quality (IQ, FWHM of the seeing disk) for each cluster and filter. If there are more than 20 exposures with IQ<0.8", we combine all exposures that satisfy this limit.

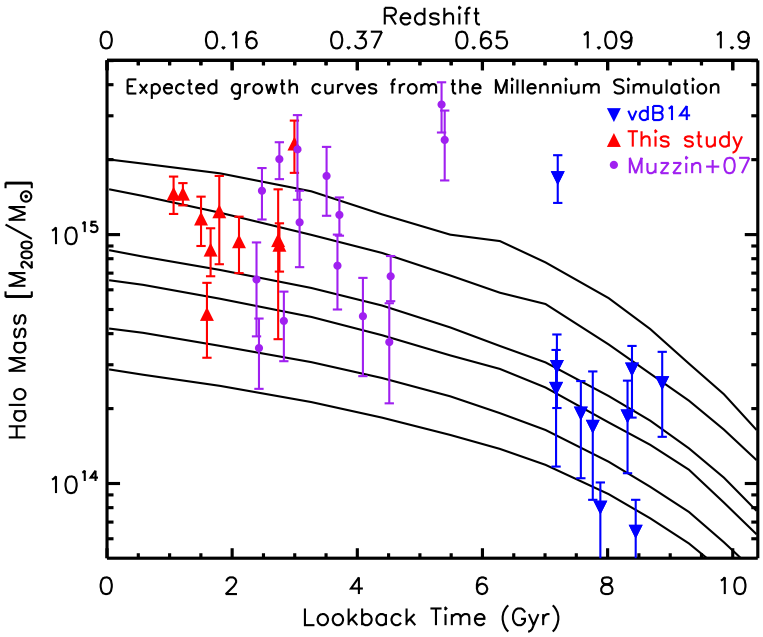

Figure 5.1: *Lines*: Expected growth curves as a function of cosmic time (or redshift) for massive haloes based on the Millennium simulation (Springel et al. 2005), in which we followed these haloes at fixed comoving number density. *Blue*: The GCLASS cluster sample studied in vdB14. *Red*: Low redshift cluster sample studied here. *Purple*: The CNOC1 cluster sample studied by Muzzin et al. (2007). The cluster samples are linked by the evolutionary growth curves.

5.2.2 Photometry - WFC

The Wide-Field Camera (WFC) is an optical mosaic camera consisting of 4 chips, which is mounted on the Isaac Newton Telescope (INT) on La Palma. Its field-of-view (FoV) is roughly 30×30 arcmin, which includes spaces between chips, see the upper left panel of Fig. 5.2. The FoV of the mosaic is smaller than MegaCam, and also does not entirely cover the full extent of the low-z clusters within their projected virial radii. In order to study the distribution and properties of galaxies that extend at least up to the cluster virial radii, we apply a dithered pointing strategy. The angular size of the virial radius depends both on the cluster total mass and its angular diameter distance (through redshift). Our approach is to take 7, 9 or 12 pointings per cluster, depending on their angular sizes. Based on an automated test of 80,000 different pointing configurations we found that these can be combined to cover >98% of the area contained within projected radii of 1000", 1200" and 1400" (respectively) from their centres to a stacked depth of at least 3 pointings, see Fig. 5.2. By

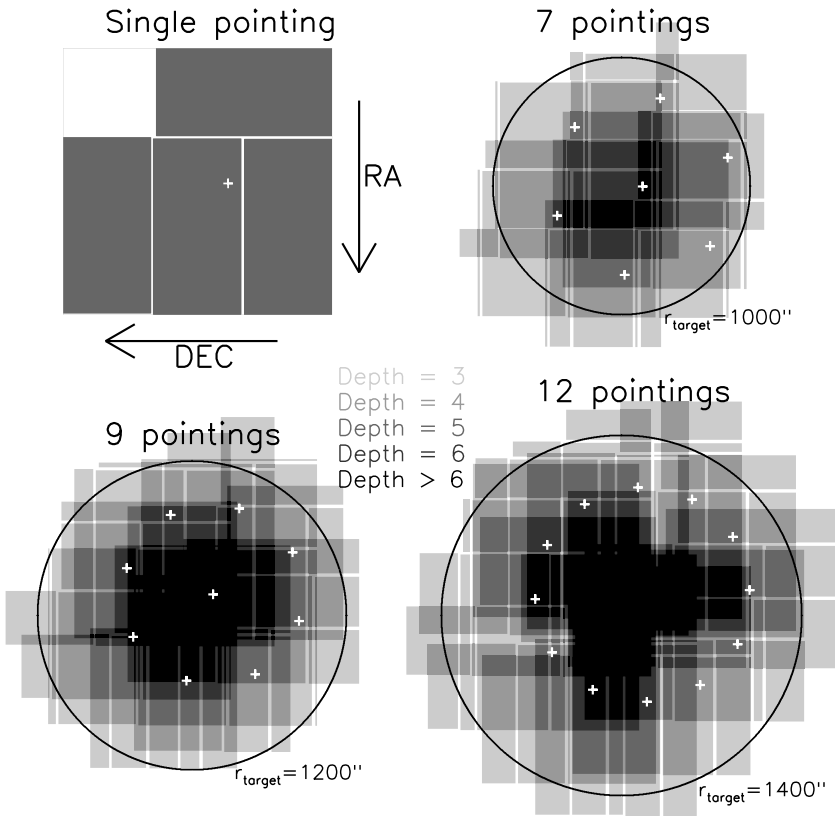

Figure 5.2: Upper left panel: Four CCDs in the WFC mosaic, showing gaps between chips. Other panels: Our optimised pointing strategy (other angular scale than upper left panel), showing how we cover the area within the estimated virial radius by using 7, 9 or 12 dithers. The area where the depth is at least 3 pointings, corresponding to a 1200s integration, is marked.

using exposure times of 400s in the u- and i-band, we reach a depth of at least 1200s over (practically) the entire cluster virial radius. Near the cluster centres there are more overlapping pointings which further enhance the depth. Since the MENeaCS and CCCP cluster samples are spread in RA, we have to combine data from observing runs in different seasons. We compiled a data set, totalling 53 nights, see Table 5.2.

Whereas we used pre-processed MegaCam data from the *Elixir* pipeline, there is no similar alternative for WFC. We therefore composed our own reduction pipeline aimed at producing images to measure fluxes in the u-, and i-bands with high photometric accuracy and precision. In summary, we construct calibration frames for each run to subtract the bias, divide through

Table 5.2: Scheduled observations on the Isaac Newton Telescope (INT) in La Palma, using the Wide Field Camera (WFC) for a total of 53 nights.

Year	Month	Days	Number of nights
2010	Jan	5-13	9
2010	Apr	14-18	5
2010	May	6-15	10
2010	Oct	7-14	8
2010	Nov	8-14	7
2011	Apr	4-7, 30	5
2011	May	1-9	9
Total			53

flat-fields, and remove fringing patterns from the i-band. We identify and mask pixels that have a nonlinear response to incoming flux, and further remove cosmic rays by using the Laplacian Cosmic Ray Identification method (van Dokkum 2001). We construct a World Coordinate System (WCS) for each image by comparing with catalogues constructed using the MegaCam data for these cluster fields. The astrometric residuals have a low scatter that is typically 0.03-0.15", consistent with statistical uncertainties in centroid determination. We perform a chip-by-chip background subtraction after masking all detected objects.

Similar to what was done for the MegaCam data, we convolve the images with a position-dependent kernel to homogenize the PSF to a circular Gaussian. The FWHM size of this Gaussian for the WFC data is larger than for the MegaCam images, typically around 2". Relative scaling of the photometric zero point between exposures is determined by considering objects that are imaged on overlapping parts between exposures. After these steps, we achieve a systematic uncertainty on flux measurements smaller than 1% in the two bands.

5.2.3 Catalogue construction

Thus far, the photometric flux measurements have been scaled to yield a uniform zero point for each filter. To convert the flux measurements in different filters to the same relative photometric scale, we exploit the universal properties of the stellar locus. This method is described in High et al. (2009), and we also applied this calibration technique to the GCLASS data (see vdB13, Appendix A). Figure 5.3 demonstrates this technique for the four bands available to us, after selecting stars based on their measured flux and angular size.

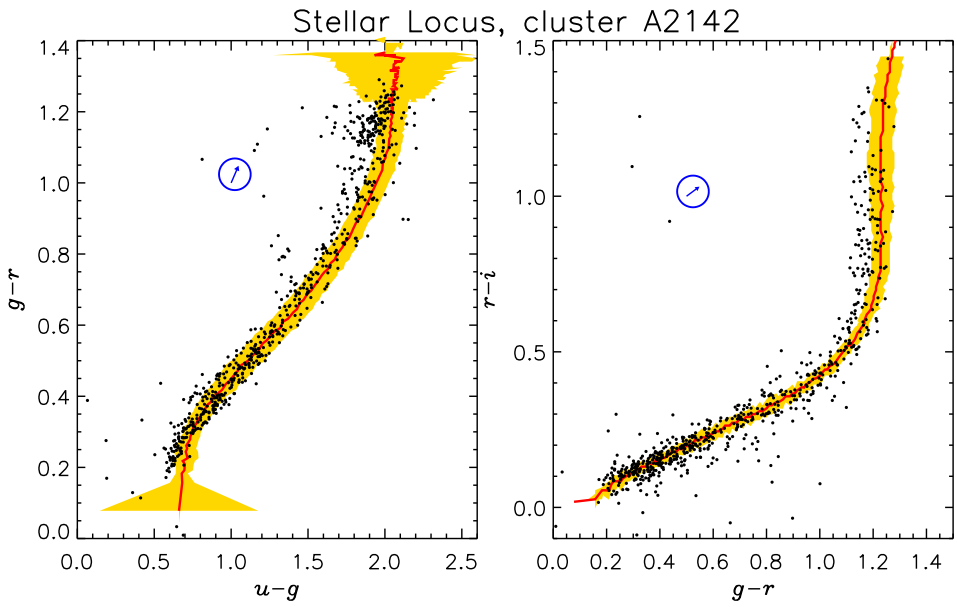

Figure 5.3: The stellar locus in 2 panels, combining the ugr *(left panel)* and gri *(right panel)* aperture fluxes of stars. *Red lines and orange contours*: colours of stars and 1-σ region of intrinsic scatter in the Covey et al. (2007) catalogue, converted to the CFHT filter set. *Black points*: colours of stars in the field of Abell 2142 after calibration. *Blue arrow*: Galactic dust reddening vector for this field.

The red line and associated 1-σ region of intrinsic scatter (orange) are based on the Covey et al. (2007) catalogue of stellar colours. Since this reference stellar catalogue is based on the SDSS filter system, we use linear colour terms to convert it to the CFHT filter set[2]. Colour terms result in rotations and transformations of the stellar locus in this colour-colour plane, and can therefore be obtained from the distribution of stellar colours itself. We estimate the following linear colour term to put the WFC measurements onto the MegaCam photometric system.

$$u_{\rm MegaCam} = u_{\rm WFC} - 0.150 \cdot (u_{\rm WFC} - g_{\rm MegaCam}) \quad (5.1)$$
$$i_{\rm MegaCam} = i_{\rm WFC} - 0.120 \cdot (r_{\rm MegaCam} - i_{\rm WFC}) \quad (5.2)$$

We use maps from Schlegel et al. (1998) to find the average extinction caused by dust in the Milky Way that is obscuring each cluster. Since the flux extinction is wavelength dependent, we estimate the extinction in each band

[2]http://www3.cadc-ccda.hia-iha.nrc-cnrc.gc.ca/megapipe/docs/filters.html

separately and correct the fluxes for this effect. The complication is that the stars in the field will have a range of distances to Earth, and thus stars that are further away have a larger amount of dust obscuration. Since we consider stars in a fixed window of apparent magnitude (e.g. $18 < \mathrm{mag}_r < 20$), we expect the redder stars to be more nearby and thus be mostly in front of the dust column. Bluer stars on the other hand have a higher luminosity and therefore are typically at a larger distance from Earth. In Fig. 5.3 the dust reddening vector is indicated in both panels, and the stars at the red (upper right) part of the stellar locus have been over-corrected for Galactic dust extinction. However, the extragalactic sources in which we are interested are corrected properly for dust. In fields that are not significantly obscured by Galactic dust (i.e. when at high Galactic latitude) the stellar locus calibration technique works best, since the shape of the stellar locus will be least affected.

The MegaCam r-band is calibrated in absolute terms with respect to standard star fields, and most of these data are taken under photometric conditions. Therefore we adjust the u-, g-, and i-band zero-points to bring the stars in the field in line with the stellar locus, and we keep the r-band zero-point unchanged. We can test the robustness of the r-band absolute calibration in the following way. We correct the zero-points in each WFC exposure for differences in exposure time and airmass (using as reference 400s and an airmass of 1.3). This gives an indication of the atmospheric transmission, which we plot as a function of time (JD). Since many clusters were observed in the same night, and in most nights the conditions changed very gradually, outliers in these diagrams are indicative of problems in absolute calibration. For example, if for a given cluster the estimated atmospheric transmission is systematically off-set for all exposures in both filters, this is a strong indication of a calibration problem. We use this information to fine-tune the zero-points further. For fields that suffer from a large Galactic dust column this is our main method for photometric calibration. The apparent magnitude after atmospheric extinction is given by $\mathrm{m} = \mathrm{m}_1 + \mathrm{k}_\lambda \times (\mathrm{airmass} - 1)$, where m_1 is the magnitude for a reference airmass of 1, and k_λ is the wavelength dependent extinction coefficient. The atmospheric extinction coefficients in the u-, and i-band we find to be 0.50 and 0.06, respectively.

Because of the excellent image quality and depth in the MegaCam r-band stacks, we use these as our detection images. For galaxies with redshift $z \lesssim 0.4$ the r-band filter probes the rest-frame SED redward of the 4000Å break, which makes the observed r-band flux a reasonable proxy for stellar mass. We measure aperture fluxes in the seeing-homogenized images using a Gaussian weight function, which we adjust in size to account for different PSF sizes. To estimate errors on these measurements, we randomly place apertures with the same shape on the seeing-homogenized images and measure the dispersion in the background. Since the flux measurements of our faint sources are background-noise limited, this way we probe the dominant component of the aperture flux

Table 5.3: The photometric data set used in this study. Unless indicated otherwise, u-, and i-band photometry is obtained using the Wide Field Camera at the INT, and g-, and r-band photometry comes from MegaCam at the CFHT. The limiting magnitudes reported are median 5-σ flux measurement limits for point sources measured with a Gaussian weight function. For all clusters apart from A655, we had to expand the size of the Gaussian aperture weight function substantially to accommodate the INT image quality.

Name	$u_{\rm lim}$ [$\rm mag_{AB}$]	$g_{\rm lim}$ [$\rm mag_{AB}$]	$r_{\rm lim}$ [$\rm mag_{AB}$]	$i_{\rm lim}$ [$\rm mag_{AB}$]
A655	25.9[a]	26.0	25.5	25.0[a]
A1033	24.0	25.0	24.4	22.9
A1068	24.8	25.1	24.4	23.6
A1835	24.5	24.8	24.4	23.6
A1914	24.0	25.1	24.5	23.2
A2029	24.2	24.6	24.0	23.4
A2069	24.0	25.1	24.5	23.2
A2111	24.4	25.2	24.6	23.1
A2142	24.3	24.8	24.2	22.5
A2261	24.3	25.0	24.4	21.8
COSMOS	26.6[a]	26.3[b]	26.4[b]	26.0[b]

[a] MegaCam, Canada-France-Hawaii Telescope (CFHT)

[b] SuprimeCam, Subaru

error. For the WFC data we compare aperture flux measurements for each source in the individual exposures and (through sigma-clipping) combine this into a flux measurement and error. Using these estimated errors we give the median depth of each image in Table 5.3, considering only positions where the image depth is at least 1200s. Note that the 5-σ depth in these apertures is also affected by the seeing in the WFC images, since the sizes of the apertures need to be expanded proportionally to the images with inferior IQ. Note that for cluster Abell 655 we have deep 4-band coverage with CFHT MegaCam.

We mask stars brighter than V=15 (automatically selected from the Guide Star Catalog II (GSC-II Lasker et al. 2008)) and their diffraction spikes and haloes in the images, which typically cover a few percent of the area. The dashed line in Fig. 5.4 shows the imaged fraction of the ensemble cluster (i.e. 10 clusters combined) on the detection images as a function of radial extent from the BCG, as scaled with the virial radius R_{200} (Table 5.1). The detection images cover an area (excluding locations with bright stars) larger than the virial radius for each cluster. We also show the fractional area covered with

4-band photometry (depth at least 1200s in each band). The inner bin is partly covered by the BCG, which does not allow for the detection of satellite galaxies, and this area is therefore also masked.

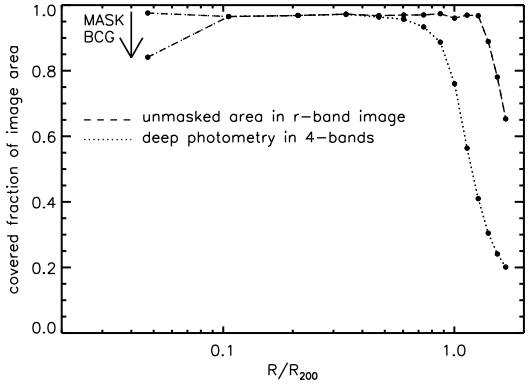

Figure 5.4: Fractionally covered area of the ensemble cluster as a function of radial distance from the BCG. *Dashed line*: imaged fraction of the ensemble cluster (i.e. 10 clusters combined) on the detection images. This excludes locations with bright stars. *Dotted line*: fractional area covered with 4-band photometry (depth at least 1200s in each band). The effective area in the inner bin is reduced due to the pixels covered by the BCG.

5.3 Analysis

We perform two parallel and (largely) independent analyses to measure the radial stellar mass distribution in the ensemble cluster. We then compare results from these analyses as a robustness test.

5.3.1 Method 1 - statistical background subtraction

The first approach is to estimate a photometric redshift for every galaxy in the cluster images, apply a cut in redshift space and statistically subtract galaxies in the fore-, and background by applying the same redshift cut to the reference COSMOS field. We use *ugri* photometric data in both our cluster fields and the COSMOS field to estimate photometric redshifts using the EAZY (Brammer et al. 2008) photometric redshift code. We use an r-band selected catalogue from the COSMOS field which has been constructed in the same way as the K-band selected catalogue of Muzzin et al. (2013b). The field has an effective area of 1.62 deg^2, and we only use data in the *ugri*-filters to provide a fair reference to our cluster sample.

Because our bluest band is the u-band, it is difficult to constrain the location of the 4000Å-break for galaxies at low ($z \lesssim 0.15$) redshift, since the break is then located in this filter. Like many redshift codes, EAZY applies a flux-, and redshift-based prior, which gives the redshift probability distribution for a galaxy of a given r-band flux P(z,r). This prior has a strong effect in estimating the most probable redshift of a galaxy when the u-g colour loses its constraining power (as is the case for redshifts $z \lesssim 0.15$). In the low redshift

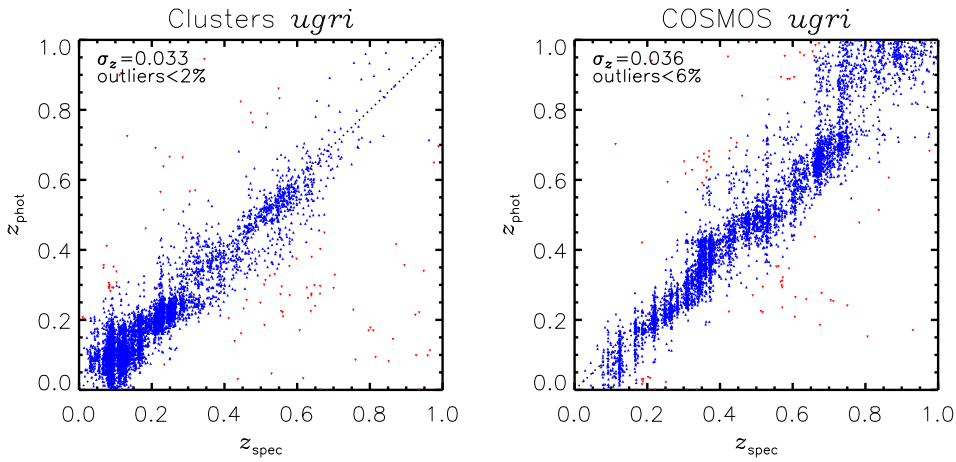

Figure 5.5: *Left panel*: Spectroscopic versus photometric redshifts for the 10 clusters in this study. Outliers, objects for which $\frac{\Delta z}{1+z} > 0.15$, are marked in red. The outlier fraction is less than 2%, the scatter (in $\frac{\Delta z}{1+z}$) of the remaining objects is $\sigma_z = 0.033$. *Right panel*: Same for the COSMOS field, but only using the $ugri$-filters. The outlier fraction and scatter are slightly larger as a result of deeper spectroscopic data (also at higher redshift where the $ugri$ filters lose their constraining power).

regime ($z \lesssim 0.3$), the comoving volume element $dV_c/dz/d\Omega$ is a strong function of redshift (e.g. Hogg 1999), but the luminosity function does not evolve strongly in this redshift range (e.g. Muzzin et al. 2013a). Therefore the prior in this regime is decreasing rapidly towards P(z,r)=0 for $z = 0$, independently of the r-band flux. Consequently, according to the prior, it is much more likely to find a galaxy at $z = 0.2$ compared to e.g. $z = 0.1$. Once a field is centred on a massive cluster at low redshift, this prior is no longer applicable since the probability of finding a galaxy to be at the cluster redshift is significantly increased. Besides the general redshift and flux-dependence of the prior, one should therefore include information on e.g. the galaxy's distance to the cluster centre to the prior. This however, is beyond our requirements, since we subtract the field statistically, and the volume (and therefore the number of contaminating galaxies) in the fields is small below $z < 0.3$. A correction on the prior will only affect redshifts at lower redshift, and will therefore not change which galaxies survive the redshift cut. For galaxies with a photometric redshift below $z_{\rm EAZY} = 0.16$ we apply a simple correction of the form photo-$z = 0.16 \cdot (z_{\rm EAZY} - 0.10)/0.06$ to the EAZY output, and plot a comparison between spec-z's and photo-z's in Fig. 5.5. We apply the same correction to the EAZY output on the COSMOS catalogue.

Since the distance modulus is a strong function of redshift in this regime, a small uncertainty in photometric redshift will result in a relatively large un-

certainty in luminosity (or stellar mass) of a galaxy. Given that the cluster redshift is well-known, we will assign the distance modulus of the cluster to every galaxy in the cluster fields. In order to properly subtract contaminating fore- and background galaxies, we also assign this distance modulus to each galaxy in the reference COSMOS field (after applying the redshift cut). We then use the SED-fitting code FAST (Kriek et al. 2009) to estimate the stellar-mass-to-light ratio (M/L) (in the r-band) for each galaxy. For this we again assume the same redshift and distance modulus (corresponding to the cluster) for each galaxy. Then in each of the radial bins (which are scaled by the size R_{200} of each cluster) we measure the area (in angular size) that is not masked by bright stars (which is also different for each cluster through its angular diameter distance) and estimate the expected number of sources in this area in the COSMOS field. We estimate the total stellar mass and corresponding error for those sources by performing a series of 10,000 Monte-Carlo realisations of the background, by randomly drawing sources from the COSMOS catalogue. We subtract the estimated field values from the raw number counts to obtain the cluster stellar mass density profile. In Appendix 5.A we perform a consistency check of this method by considering the stellar mass distribution of galaxies located far away from the cluster centre and comparing this to the field stellar mass distribution. We find no significant systematic difference between the field probed around the cluster and the reference COSMOS field, which strengthens our confidence in this method.

5.3.2 Method 2 - spectroscopic approach

In the method described above, we subtract the galaxies in the fore-, and background statistically based only on the photometric data. However, as discussed in Sect. 5.2, we can use a substantial amount of spectroscopic redshifts in the cluster fields from the literature. In this second approach we measure the stellar mass contained in spectroscopically confirmed cluster members to provide a lower limit to the full stellar mass distribution.

Since the spectroscopic data set is obtained after combining several different surveys, the way the spectroscopic targets have been selected is not easily reconstructed. Fig. 5.6 shows the spectroscopic completeness for all galaxies with a photometric redshift $z < 0.3$ as a function of stellar mass (assuming the same distance modulus as the cluster redshift), and for different radial bins. For stellar masses $\mathrm{M}_\star > 10^{11}\,\mathrm{M}_\odot$, the completeness is very high ($> 80\%$). Since these objects constitute most of the total stellar mass distribution (see vdB14 (Fig. 2) for this argument), we can get a fairly complete census of stellar mass by just considering the galaxies for which we have a spectroscopic redshift. Note however that the stellar mass contained in the spectroscopically confirmed members is a lower limit to the total, but since the spectroscopic completeness is not a strong function of radial distance, we expect to miss

a similar stellar mass fraction at different distances. We obtain stellar mass estimates for these spectroscopically confirmed cluster galaxies using the SED fitting code FAST. We run 10,000 Monte-Carlo realisations in which we randomly draw spectroscopic members in each bin to estimate the 1-σ statistical uncertainty on each data point.

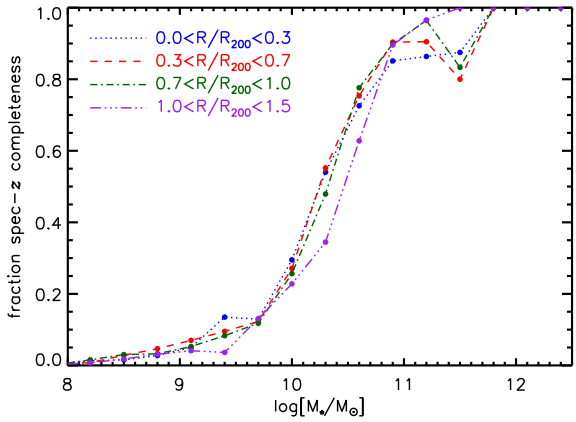

Figure 5.6: Spectroscopic completeness for sources with a photometric redshift $z < 0.3$ as a function of stellar mass (assuming the same distance modulus as the cluster redshift). The four lines show different radial bins. The completeness is similar for each bin, and is larger than 80% for stellar masses $\mathrm{M}_\star > 10^{11}\,\mathrm{M}_\odot$.

5.4 Results and comparison at low-z

In this section we present the galaxy number and stellar mass density distributions of the 10 clusters we study, based on the two independent analyses described in Sect. 5.3. We compare these results to literature measurements at comparable redshifts ($z < 0.3$). In Sect. 5.5 we discuss a possible evolutionary scenario by comparing these results to measurements at higher redshifts.

5.4.1 Galaxy number density profile

Ignoring baryonic physics, the galaxy number density distribution in cluster haloes can be compared to the distribution of sub-haloes in N-body simulations as a test of ΛCDM. Due to mergers and interactions between galaxies, the number density distribution of galaxies may be different for galaxies with different stellar masses. Figure 5.7 shows the projected galaxy number density distribution for galaxies with stellar masses exceeding $\mathrm{M}_\star > 10^9\,\mathrm{M}_\odot$ (left panel), and $\mathrm{M}_\star > 10^{10}\,\mathrm{M}_\odot$ (right panel) in the ensemble cluster. These cuts are chosen to facilitate comparisons with literature measurements of different depths. Before stacking the 10 clusters, their radial distances to the BCGs are scaled by R_{200}. The blue points show the raw number counts, including the field. After the field (red points) is subtracted, we obtain the black data points as our estimate for the cluster.

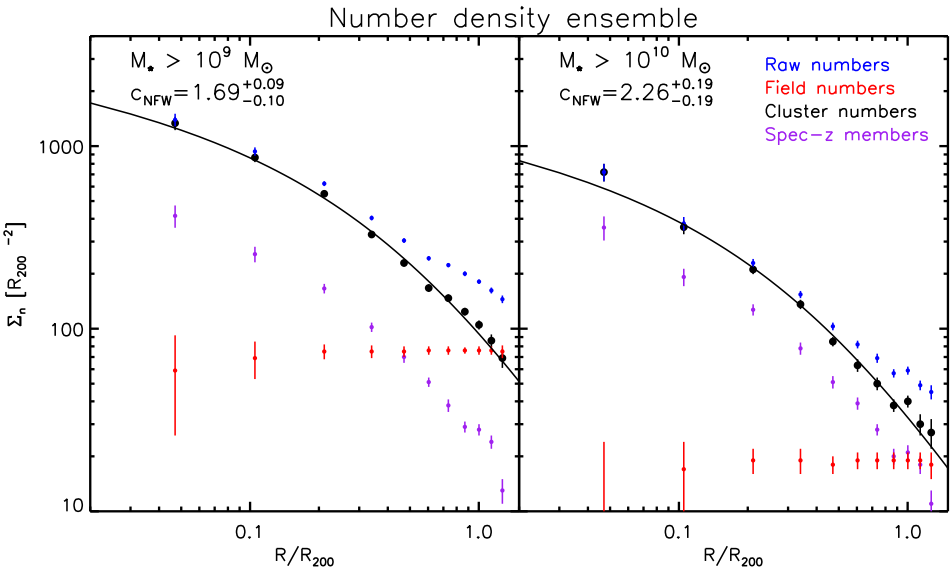

Figure 5.7: Galaxy number density distributions in the mass range $M_\star > 10^9\,M_\odot$ (left panel), and $M_\star > 10^{10}\,M_\odot$ (right panel) for the ensemble cluster at $z \sim 0.15$. Error bars give Poisson sampling errors. Black points with the best fitting projected NFW functions are our best estimate for the cluster number counts. Purple points indicate the number of spectroscopically confirmed cluster members.

We fit projected NFW profiles to the data points, minimizing the χ^2 value and taking account of the 2D annulus-shaped bins. The best fitting functions give reasonable fits to the data (see the reduced χ^2 values in Table 5.4). We give the best-fitting concentration parameters and their marginalized errors in the table, and show the best-fitting functions in Fig. 5.7. The purple points show the numbers of spectroscopically confirmed member galaxies.

We find a significant difference in the best fitting concentration ($1.69^{+0.09}_{-0.10}$ versus $2.26^{+0.19}_{-0.19}$) between the different (though overlapping) mass bins ($M_\star > 10^9\ M_\odot$ and $M_\star > 10^{10}\,M_\odot$, respectively), indicating that the more massive galaxies are more strongly concentrated in the cluster ensemble. The effect of dynamical friction, which is more efficient for massive galaxies, can be the cause of this mass segregation. Note that this effect is observed without taking account of the BCGs.

The number density profiles in the literature that we can compare with have been measured on shallower data. Lin et al. (2004) study the average number density profile of a sample of 93 clusters at $0.01 < z < 0.09$ with 2MASS K-band data. They are able to measure down to a magnitude limit (Vega) of $K_{s,lim} = 13.5$, which corresponds to $M_\star \approx 10^{10}\,M_\odot$ at $z = 0.05$ (Bell & de Jong 2001). Although they study systems with a lower mass range than

Table 5.4: Parameters describing the best fitting NFW profile to the radial density distributions. Reduced χ^2 values are given (10 to 12 degrees of freedom per cluster).

	Stellar Mass density		Number density $M_\star > 10^9\,M_\odot$		Number density $M_\star > 10^{10}\,M_\odot$	
Cluster	$c_{\rm NFW}$	$\chi^2/d.o.f.$	$c_{\rm NFW}$	$\chi^2/d.o.f.$	$c_{\rm NFW}$	$\chi^2/d.o.f.$
A655	$2.83^{+0.76}_{-0.66}$	1.19	$3.78^{+0.52}_{-0.47}$	1.53	$3.68^{+0.90}_{-0.71}$	0.65
A1033	$5.53^{+2.42}_{-1.71}$	1.08	$3.49^{+0.76}_{-0.67}$	1.39	$4.16^{+1.52}_{-1.19}$	0.83
A1068	$1.07^{+0.71}_{-0.47}$	0.76	$1.21^{+0.57}_{-0.38}$	2.13	$1.16^{+0.57}_{-0.43}$	1.01
A1835	$3.35^{+0.90}_{-0.71}$	1.73	$1.97^{+0.29}_{-0.28}$	3.42	$3.25^{+0.71}_{-0.57}$	1.67
A1914	$5.44^{+2.28}_{-1.85}$	0.95	$3.02^{+0.48}_{-0.47}$	2.27	$4.35^{+1.33}_{-1.14}$	0.77
A2029	$0.88^{+0.43}_{-0.24}$	0.63	$1.21^{+0.19}_{-0.19}$	0.46	$1.40^{+0.38}_{-0.38}$	0.84
A2069	$1.74^{+0.62}_{-0.48}$	1.29	$1.40^{+0.24}_{-0.28}$	1.10	$2.07^{+0.71}_{-0.52}$	0.98
A2111	$3.87^{+1.28}_{-1.04}$	0.82	$2.45^{+0.43}_{-0.38}$	0.26	$2.73^{+0.81}_{-0.57}$	0.57
A2142	$0.93^{+0.28}_{-0.24}$	0.33	$0.83^{+0.14}_{-0.14}$	0.88	$1.21^{+0.33}_{-0.28}$	0.90
A2261	$1.69^{+0.43}_{-0.29}$	0.84	$1.88^{+0.29}_{-0.19}$	0.89	$2.21^{+0.52}_{-0.43}$	0.59
ensemble	$1.92^{+0.19}_{-0.14}$	0.81	$1.69^{+0.09}_{-0.10}$	1.74	$2.26^{+0.19}_{-0.19}$	1.40

we probe, they find a number density concentration of $c = 2.90^{+0.21}_{-0.22}$, which is comparable to the value of $c = 2.26^{+0.19}_{-0.19}$ that we find for the high mass galaxies ($M_\star > 10^{10}\,M_\odot$).

Budzynski et al. (2012) measure the radial distribution of satellite galaxies in groups and clusters in the range $0.15 < z < 0.40$ from the SDSS DR7. For the satellite galaxies they apply a magnitude limit of $M_r = -20.5$. This corresponds to about $M_\star = 10^{10.5}\,M_\odot$ for galaxies with a high M/L. The best fitting concentration parameter of $c \sim 2.6$ they find is also consistent with our measurement for the high-mass sample. They find that the concentration of satellites falls slightly as their brightness increases, but note that they compared satellites in a higher luminosity range with respect to our study.

vdB14 measure the number density distribution of the GCLASS cluster ensemble at $z \sim 1$ down to a stellar mass of $M_\star = 10^{10.2}\,M_\odot$. They measure an NFW concentration parameter of $c = 5.14^{+0.54}_{-0.63}$, which is significantly higher than the value we find for the low-z sample. A comparison between the number density distribution and the stellar mass density distribution presented in vdB14 suggests that the more massive galaxies are situated closer towards the cluster centres than lower mass galaxies, which is qualitatively consistent with the trend we find here.

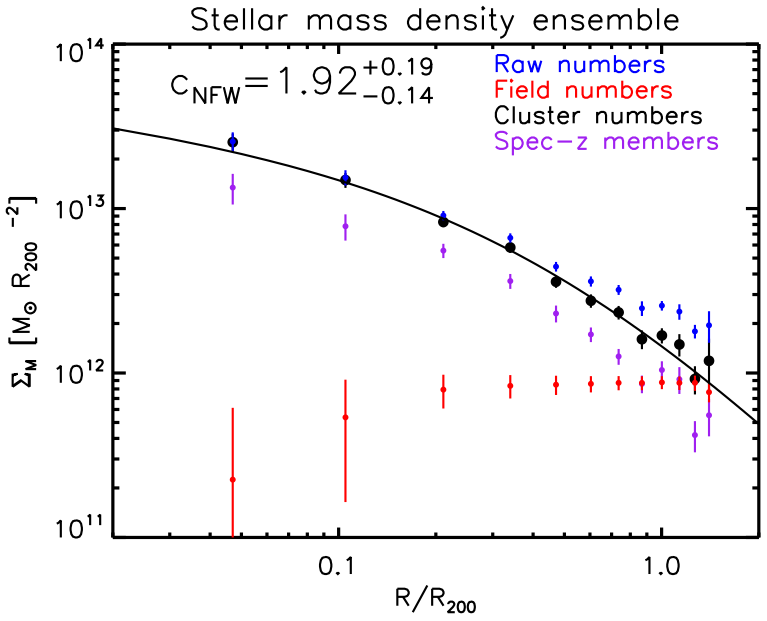

Figure 5.8: Stellar mass density distribution of the ensemble cluster at $z \sim 0.15$. Black points with corresponding Poisson sampling errors are our best estimate for the cluster stellar mass distribution. The best fitting projected NFW function is also shown. The purple points give the stellar mass distribution in spectroscopically confirmed cluster members.

5.4.2 Stellar mass density profile

Whereas the number density of galaxies can change as a result of mergers, the stellar mass density is not immediately affected by such processes if we ignore the build-up of ICL and stellar mass in the central galaxies, because these components are not included in these profiles. Figure 5.8 shows the radial distribution of stellar mass in the ensemble cluster. Radial distances are normalised by the clusters' scale radii R_{200}. Black data points give the background-subtracted (i.e. blue minus red) cluster stellar mass distribution. Errors are Poisson sampling errors, compared to which the stellar mass errors of individual galaxies can be ignored. The purple points show the numbers of spectroscopically confirmed member galaxies. The spectroscopic completeness in terms of total stellar mass is larger than 50%, and does not significantly depend on radial distance (cf. Fig. 5.6). Stellar mass distributions for individual clusters are presented in Figs. 5.9 & 5.10.

We fit a projected NFW profile to the black data points, minimizing the χ^2 value and taking account of the 2D annulus-shaped bins. The best fitting function gives a reasonable fit to the data (see the reduced χ^2 value in Table 5.4).

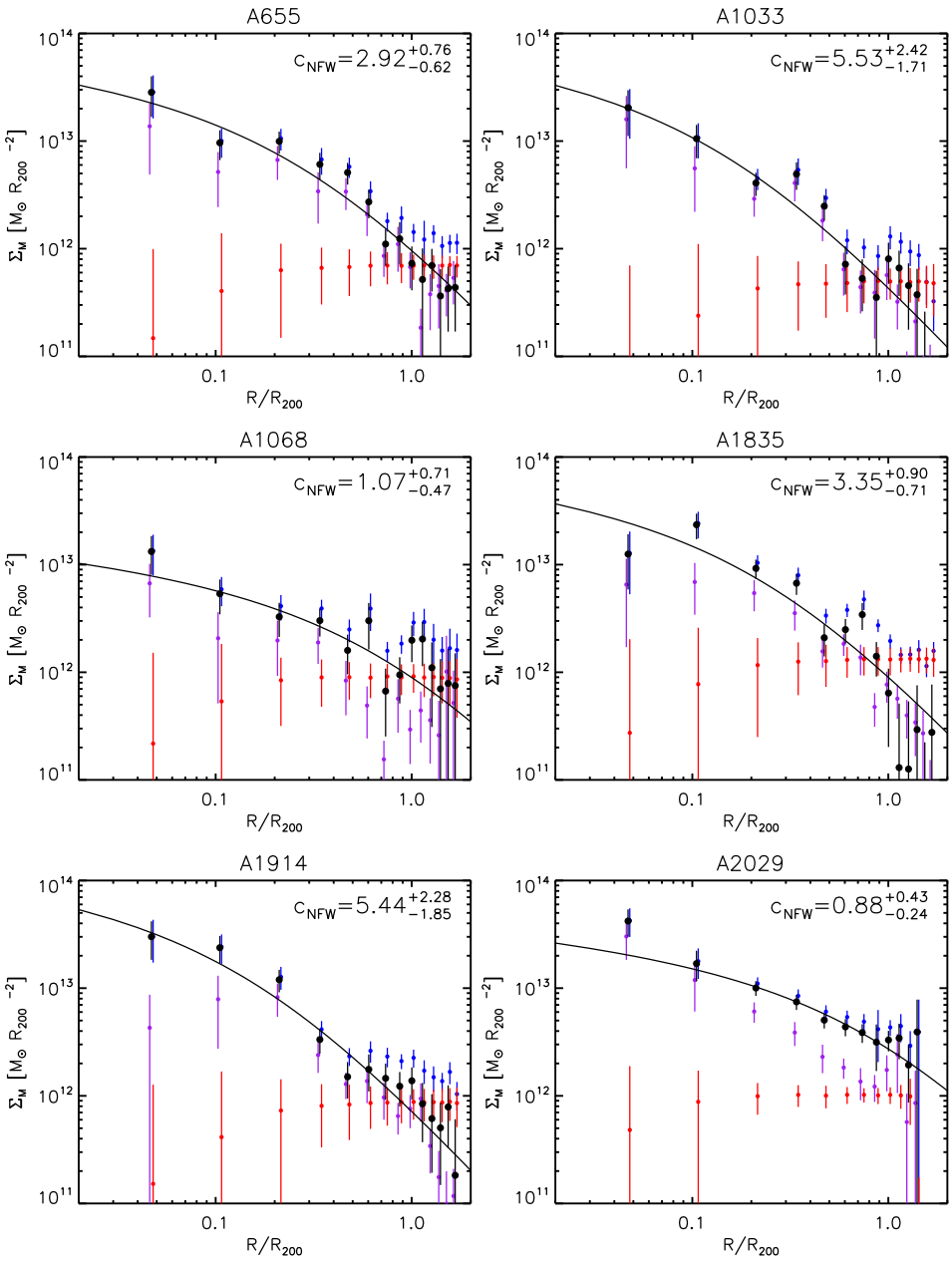

Figure 5.9: Stellar mass density distribution of the individual clusters. Black points with corresponding Poisson sampling errors are our best estimate for the cluster stellar mass distribution. The best fitting projected NFW functions are also shown. The purple points give the stellar mass distribution in spectroscopically confirmed cluster members.

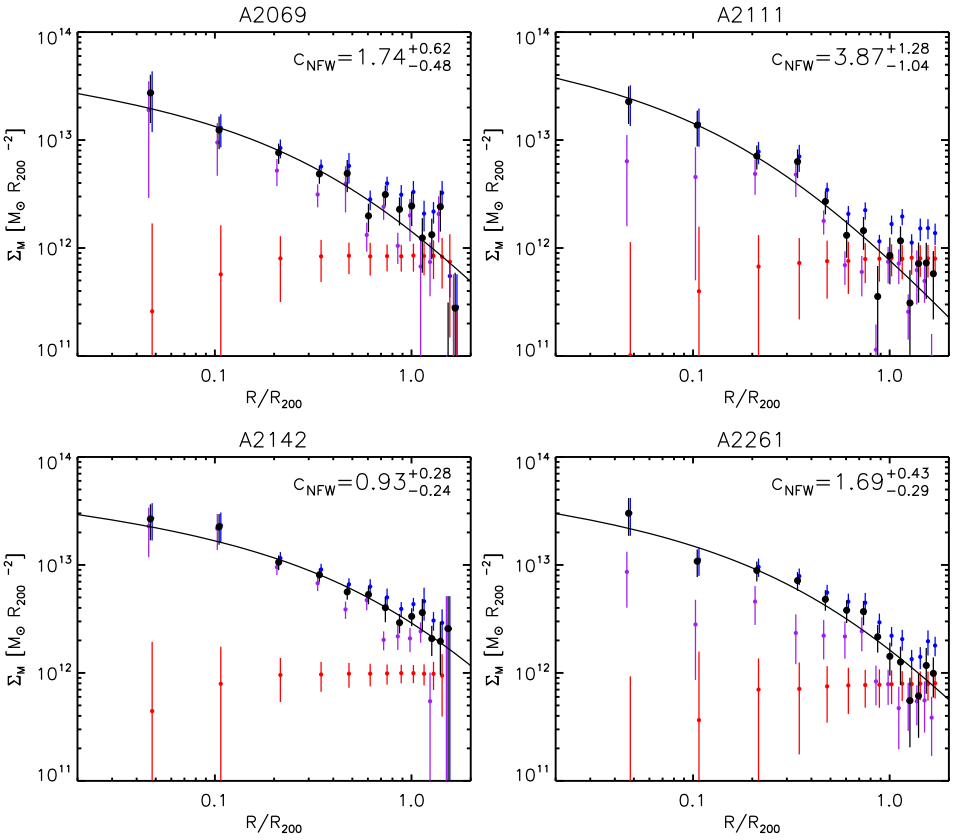

Figure 5.10: Figure 5.9 continued...

The best fitting concentration parameter for the ensemble is $c = 1.92^{+0.19}_{-0.14}$. Errors on this parameter are marginalized over the normalisation, and the best fitting NFW profile is shown in Fig. 5.8. When we fit a projected NFW profile to the spectroscopic data (purple points) we find $c = 2.21^{+0.19}_{-0.28}$, which agrees to within 1-σ with the photometric estimate. The normalisation is different by 0.22 dex. The fact that the background subtraction method yields the same concentration parameter is a strong robustness test.

We also fit projected NFW profiles to the stellar mass distributions for the individual clusters (Figs. 5.9 & 5.10), and present the best-fitting concentration parameters in Table 5.4. Although the uncertainties on the concentration parameters are relatively large due to lower number statistics compared to the ensemble, the scatter between the individual measurements seems to be larger than the measurement errors. Some sources of this intrinsic scatter are probably different orientations on the sky, centroiding uncertainties and

different halo mass assembly histories for the clusters. We measure the intrinsic scatter in the concentration parameter by minimizing the log-likelihood

$$-2\ln\mathcal{L} = 2\sum_{i=1}^{n}\ln w_i + \sum_{i=1}^{n}\left(\frac{c_i - c_{\rm ensemble}}{w_i}\right)^2, \tag{5.3}$$

where index i runs over the 10 clusters in our sample, and where w_i is a combination of statistical uncertainties on each individual measurement and a Gaussian intrinsic scatter $\sigma_{c,\rm int}$, such that $w_i = \sqrt{\sigma_{c,i}^2 + \sigma_{c,\rm int}^2}$. See also Hoekstra et al. (2011) for a comprehensive description of this method to estimate the intrinsic scatter. We find an intrinsic scatter in the concentration parameter of $\sigma_{c,\rm int} = 0.70^{+0.33}_{-0.22}$ (or $\sigma_{\log_{10}c,\rm int} = 0.25 \pm 0.05$ dex).

Muzzin et al. (2007) measure the K-band luminosity profiles for a stack of 15 CNOC1 (Yee et al. 1996) clusters in the redshift range $0.2 < z < 0.5$. In this redshift range, the luminosity in the K-band is expected to be a good proxy for stellar mass. They find a concentration of the luminosity density of $c = 4.28 \pm 0.70$. Although the redshift range of the CNOC1 sample is different from ours, they are approximate progenitors of the sample we study (see Fig. 5.1).

In vdB14 we present the stellar mass density distribution of the GCLASS cluster sample at $z \sim 1$, and find a relatively high concentration of $c = 7.12^{+1.53}_{-0.99}$. These systems are likely to grow into clusters that are only a factor of ~ 2 less massive than the low-z clusters studied in this paper. Comparisons among these results indicate that the stellar mass distribution in clusters evolves significantly over cosmic time.

5.5 The evolving stellar mass distribution

We have performed a measurement of the stellar mass distribution in clusters in the local ($0.07 < z < 0.26$) Universe. In Fig. 5.11 we compare this measurement to results from the GCLASS and CNOC1 surveys, which suggests that the stellar mass distribution evolves significantly between $z \sim 1$ and the local Universe.

We note that the concentration parameters we are comparing are defined with respect to the cluster scale radii R_{200}, which correspond to a physical size of ~ 1 Mpc for GCLASS, and $R_{200} \sim 2$ Mpc for the low-z sample. If the critical density $\rho_{\rm crit}$, with respect to which the scale radii are defined, evolves, the measured concentrations will change, even if the physical profile remains constant over time (pseudo-evolution, e.g. Diemer et al. 2013). Nonetheless, clusters in this mass regime ($10^{14} < M_{200}/\mathrm{M}_\odot < 10^{15}$) are expected to grow by a factor of ~ 3.0 between $z = 1$ and $z = 0$ (Wechsler et al. 2002; Springel et al. 2005). In Fig. 5.12 we compare the cluster stellar mass density profiles at the

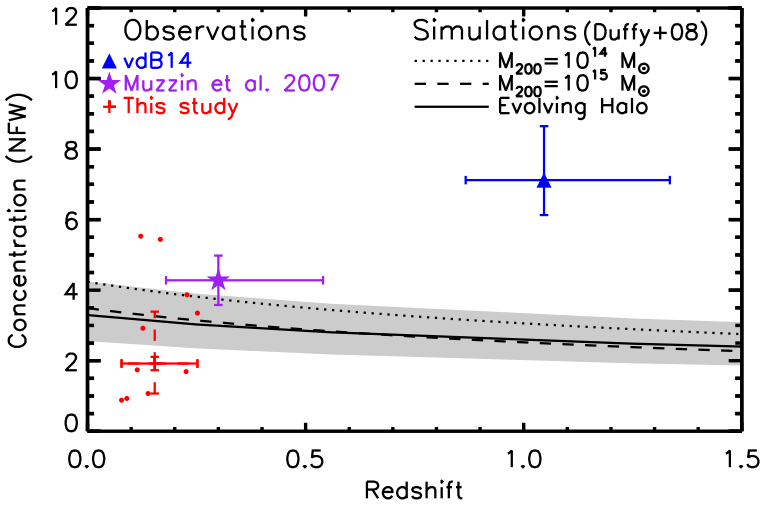

Figure 5.11: *Black lines*: The NFW concentration in the sample of relaxed haloes from Duffy et al. (2008) as a function of redshift. *Dotted and dashed*: Haloes of a given mass as a function of redshift. *Solid*: NFW concentration of a halo that is evolving in mass, with scatter given by the shaded region. The full sample from Duffy et al. (2008) has a slightly lower average concentration, but a larger scatter. *Blue*: Stellar mass density concentration in GCLASS from vdB14. *Purple*: K-band luminosity density concentration in CNOC1 from Muzzin et al. (2007). *Red*: Stellar mass density concentration for the clusters used in this study. The dashed error bar on the mean represents the best-fit log-normal intrinsic scatter on the concentration. Red points give measured concentrations for the individual clusters in MENeaCS/CCCP.

same physical scale, so that we circumvent the effect of pseudo-evolution, and study directly how the profiles of these clusters evolve since $z \sim 1$. Given that the current low-z sample is a factor ~ 1.7 more massive than the descendants from GCLASS are expected to be (see Fig. 5.1), and the relation between stellar mass and halo mass $M_\star \propto M_{500}^{0.71\pm0.04}$ from Lin et al. (2012) (also see vdB14 (Fig.5)), we multiplied the low-z profile by a factor of 0.7 to better resemble the expected descendant sample from GCLASS. The exact value of this correction factor does not have a significant impact on the interpretation.

Figure 5.12 suggests that, although the total stellar mass of these clusters grows substantially since $z \sim 1$, the stellar mass density in the cluster core (R < 0.2 Mpc) drops significantly during the same period. Since in our analysis we did not take account of the ICL component, and excluded the BCGs from the fit, the build-up of stellar mass in these components may be responsible for the observed evolution.

Massive galaxies close to the BCG are expected to merge with the central galaxy on a relatively short time-scale, and play a dominant role in the build-

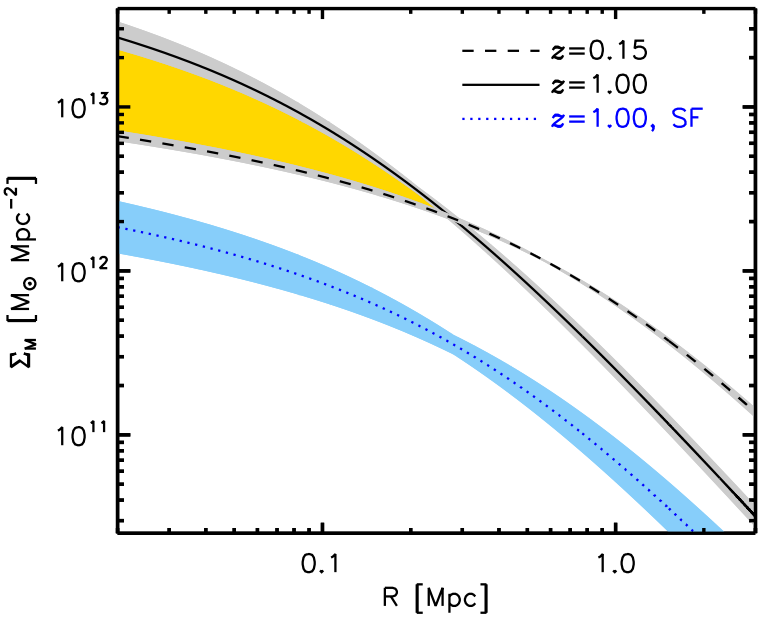

Figure 5.12: *Black solid*: The average stellar mass density profile of GCLASS, in physical units. *Black dashed*: The stellar mass density profile at low-z, at the same physical scale. *Blue solid*: The average stellar mass density profiles of the star-forming galaxies in GCLASS, which is the most recently accreted population of galaxies. Shaded regions mark 1-σ uncertainty regions on the NFW parameters. The orange region marks the part of the $z \sim 1$ profile that is in excess of the $z \sim 0.15$ profile.

up of stellar mass in the BCG (e.g. Burke & Collins 2013; Lidman et al. 2013). Several studies have found that the stellar mass in central galaxies is related to the halo mass of the system (e.g. Lidman et al. 2012; Behroozi et al. 2013, vdB14), with a relation that is aproximately $M_{\rm BCG} \propto M_{200}^{0.5}$ in this mass and redshift regime. If we integrate the mass enclosed in the $z \simeq 1$ profile that is in excess of the $z \simeq 0.15$ profile (i.e., the orange region in Fig. 5.12), we find that this is on average about $2 \times 10^{11}\,M_{\odot}$ per cluster. Given that the BCGs in the GCLASS clusters have typical stellar masses of $M_{\star,\rm BCG} \simeq 3 \times 10^{11}\,M_{\odot}$ (vdB14, Table 2), and the halo masses are expected to grow by a factor of ~ 3 since $z \sim 1$, we find that the growth of the stellar mass in the central galaxies can readily explain the decreasing profile.

Furthermore, dynamical interactions between galaxies in the cluster may lead to a build-up of the ICL component. Gonzalez et al. (2013) measure the contribution of the BCG+ICL component to the total luminosity of a sample of galaxy groups and clusters at $z \sim 0.1$ (for estimates of the ICL component, also see Zibetti et al. 2005; Sand et al. 2011). Gonzalez et al. (2013) find that

the BCG+ICL fraction is a decreasing function of system mass (or velocity dispersion), and is about 30% of the total luminosity within R_{500} for systems with $\sigma = 1000\,\mathrm{km\,s^{-1}}$. Around $z \sim 1$, the stellar mass fraction in the ICL is expected to be significantly lower (Burke et al. 2012) (this trend is also reproduced with semi-analytic models, Contini et al. (2013)). The development of an ICL component may therefore also contribute to an evolution in the observed stellar mass density profile.

Substantial growth onto the outskirts of the clusters is also required to explain the observed evolution since $z \sim 1$. In Fig. 5.12 we show the stellar mass density profile of the star-forming galaxies in GCLASS, which are expected to be accreted from the field relatively recently compared to the more concentrated quiescent population (vdB14). Given that this population is described by a radial distribution that is similar in shape to the total stellar mass distribution at lower redshift, a continuation of star-formation and accretion at these locations could explain the stellar mass density evolution on the outskirts.

Under the assumption that galaxies populate sub-haloes and that these systems are accreted onto the clusters since $z = 1$, it is expected that dark-matter haloes also accrete matter onto the outskirts. This effect is indeed observed in N-body simulations (Duffy et al. 2008), if these simulations are compared on the same physical scale. The substantial difference between the concentration simulated with N-body codes and the observed distribution of stellar mass may be reconciled by modifying the stellar mass fraction of infalling haloes in semi-analytic models. The observed evolution of the stellar mass distribution is also a stringent test for existing and future hydrodynamical simulations (e.g. Schaye et al. 2010; Cen 2014).

5.5.1 Selection effects in GCLASS

Given the significant evolution that is observed between the GCLASS sample and the low-z descendant sample, we have to consider the possibility that this inferred evolution is caused by the way these samples are selected. Since it is impossible to select a cluster sample based on halo mass, different selection methods (X-ray, SZ-, or galaxy selections) potentially result in a biased sample of clusters.

The GCLASS sample consists of 10 clusters drawn from the 42 degree Spitzer Adaptation of the Red-sequence Cluster Survey (SpARCS, Muzzin et al. 2009; Wilson et al. 2009; Demarco et al. 2010). Clusters in SpARCS were detected using the red-sequence detection method developed by Gladders & Yee (2000), and expanded on in Muzzin et al. (2008). In summary, this detection method was applied to the optical+InfraRed data in SpARCS, so that the $z' - 3.6\mu$m colour was used to detect clusters at redshifts $z > 0.8$ after convolving the galaxy number density maps with an exponential kernel (see

Gladders & Yee 2000, Eq. 3). Richnesses were measured in fixed apertures with a radius of 500 kpc, after which the richest systems were considered for follow-up photometry and spectroscopy. Muzzin et al. (2012) describes how this GCLASS follow-up sample was drawn from the richest systems after optimising the redshift baseline and ensuring a spread in RA for observational convenience. The fixed aperture of 500 kpc makes the richness selection independent on concentration. However, we have to explore the possibility that richness and concentration are correlated quantities such that a richness selection indirectly biases our sample towards high/low concentrations.

The statistics in the GCLASS sample are insufficient to study a possible trend between richness and concentration at $z \sim 1$. Therefore we examine this using the low-z sample, for which we are able to measure a concentration for each individual cluster. Although the current sample of 10 clusters is limited, we find a hint of a correlation between richness (measured by counting all galaxies more massive than $M_\star > 10^{10}\,\mathrm{M}_\odot$ within a radius of $1.2\,R_{200}$, background subtracted) and concentration, with a Spearman rank coefficient of $\rho = -0.62$. This negative correlation may not come as a surprise given the known mass-concentration relation (e.g. Comerford & Natarajan 2007; Mandelbaum et al. 2008), and mass-richness relation (e.g. Andreon & Hurn 2010; Bauer et al. 2012). Specifically, the two richest systems (A2142 and A2029) appear to have the lowest concentrations. Therefore, if the same is true at higher redshift, the current sample does not support the idea that a richness selection would result in a cluster sample with stellar mass distributions that are highly concentrated. We will expand the sample to 30-40 clusters, which will allow us to study a possible correlation between richness and concentration for clusters in similar (dynamical) mass bins.

In this thesis, we proceed to test a potential bias in the selection of GCLASS by comparing the dynamical masses of the GCLASS sample to the Tinker et al. (2008) cumulative halo mass function based on a WMAP7 cosmology, which we do in Fig. 5.13. Given the effective area of 41.9 square degrees we estimate the effective volume of the SpARCS survey (from which GCLASS was selected) in the redshift slice $0.86 < z < 1.34$ and normalise the cumulative number density of the GCLASS clusters over this volume. At the high-mass end of the distribution we expect Poisson scatter, and there is scatter in the mass-richness relation to be considered. The ten GCLASS systems are therefore not necessarily the most massive ones. Based on this comparison, we estimate that in GCLASS we probe around 10% of the clusters in the SpARCS volume around the median mass of the GCLASS sample ($M_{200} \simeq 10^{14.3}\,\mathrm{M}_\odot$).

We consider the possibility that the clusters probed by GCLASS are the 10% with the highest concentrations in the simulation. Figure 5.14 shows the GCLASS ensemble average stellar mass concentration with a Gaussian probability distribution around $c = 7.12$. The Duffy et al. (2008) log-normal concentration distribution for cluster-sized haloes in N-body simulations are

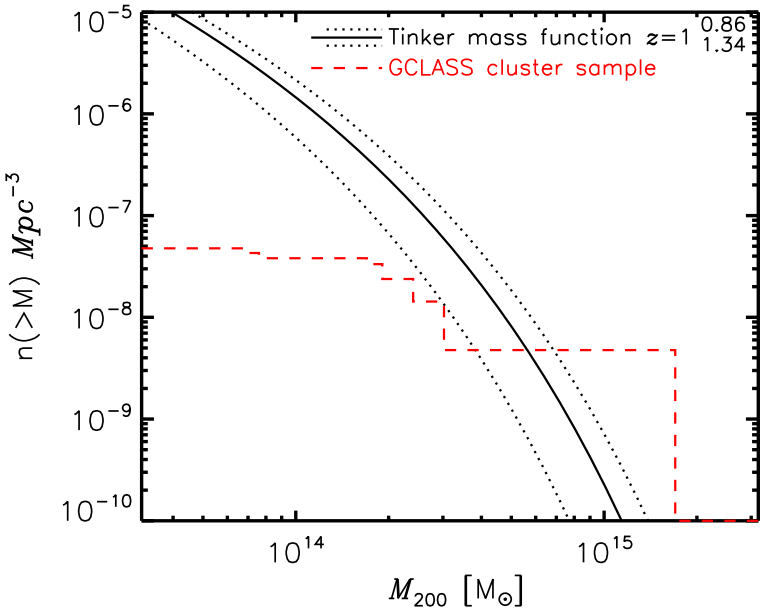

Figure 5.13: *Black solid line*: Tinker et al. (2008) cumulative mass function at $z = 1$ for WMAP7 cosmology. *Black dotted lines*: Tinker et al. (2008) cumulative mass functions at $z = 0.86$ and $z = 1.34$, which are the redshift limits within which the GCLASS clusters are selected. *Red dashed line*: cumulative mass function of the 10 GCLASS clusters, normalised by the total volume of SpARCS.

Figure 5.14: *Black solid line*: GCLASS ensemble average stellar mass concentration with a Gaussian probability distribution around $c = 7.12$. Also shown are the log-normal concentration distribution for clusters with the same mass and redshift as the GCLASS sample for the relaxed haloes in Duffy et al. (2008) (*Blue dotted line*), and their full sample (*Red dashed line*).

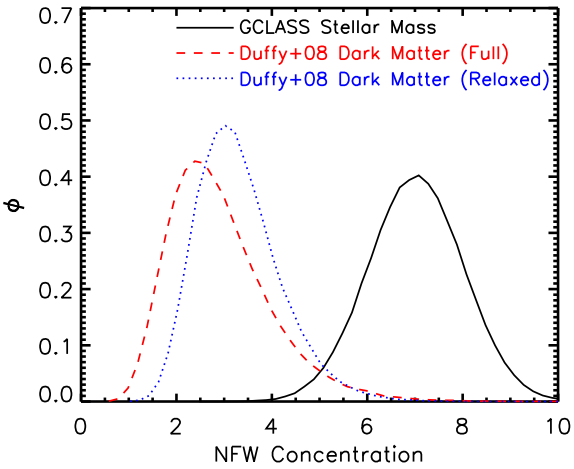

also shown, both for their relaxed and full sample (haloes were categorized based on the distance between the most bound particle and the centre of mass in the simulation). The relaxed sample has a slightly higher concentration of c=3.30 compared to c=2.84 for the full sample, but has a smaller scatter ($\sigma(\log_{10}c)$=0.11 dex versus 0.15 dex for the full sample). Where the Duffy et al. (2008) distributions overlap with the GCLASS probability distribution, these two distributions are similar.

We perform a simple test in which we randomly sample 100 concentrations from the Duffy et al. (2008) relations. We do this for 1000 different realisations and each time average the 10 most concentrated ones. In only 3% of the realisations we find a larger average than the measured concentration from GCLASS ($c = 7.12^{+1.53}_{-0.99}$), taking account also of the error on this measured concentration. Therefore, even under the most conservative assumption that a richness selection is completely biased towards the most concentrated galaxy clusters, there is only a 3% probability that we measure an average concentration for GCLASS of $c = 7.12^{+1.53}_{-0.99}$. Moreover, as we argued in vdB14, the measured concentration of $c \simeq 7.12$ is a lower limit if we include uncertainties arising from misalignments between the BCGs and the "true" cluster centres. Given these arguments, it is unlikely that both the observed evolution since $z \sim 1$, and the difference between the predictions from N-body simulations and observations at this redshift, are only an effect of the way the GCLASS sample is selected.

5.6 Summary and Conclusions

In this paper we study the radial galaxy number density and stellar mass density in a sample of 10 galaxy clusters at $0.07 < z < 0.26$. These clusters are drawn from the Multi-Epoch Nearby Cluster Survey (MENeaCS) and the Canadian Cluster Comparison Project (CCCP). Approximately 3000 member galaxies in these clusters have been identified by several spectroscopic surveys in the literature. We compiled catalogues of $ugri$-band photometry to estimate photometric redshifts and stellar masses for each cluster field.

We measure the galaxy number density distribution in two (overlapping) stellar mass bins, and find that the higher mass galaxies ($M_\star > 10^{10}\,M_\odot$) are concentrated more strongly ($c = 2.26^{+0.19}_{-0.19}$) than galaxies with masses $M_\star > 10^{9}\,M_\odot$ ($c = 1.69^{+0.09}_{-0.10}$). This observed mass segregation is expected from the process of dynamical friction. We find a qualitative agreement between these measurements and the literature measurements of galaxy distributions in low-z clusters.

We measure the radial stellar mass density profile in two ways, finding similar results (within 1-σ uncertainty). The statistical subtraction method relies exclusively on the photometric information. For the spectroscopic approach

we use the photometry only to measure stellar masses for the spectroscopically identified cluster members. The stellar mass distribution in the ensemble cluster is well fitted by a projected NFW profile with concentration $c = 1.92^{+0.19}_{-0.14}$. From the measured concentrations for the individual systems, we estimate an intrinsic scatter of $\sigma_{c,\mathrm{int}} = 0.70^{+0.33}_{-0.22}$ (or $\sigma_{\log_{10}c,\mathrm{int}} = 0.25 \pm 0.05$ dex). Some sources that may contribute to this intrinsic scatter are different orientations on the sky, centroiding uncertainties and different halo mass assembly histories for the clusters.

The cluster sample we study is close in halo mass to the likely descendant population of the $z \sim 1$ GCLASS cluster sample (vdB14), for which a stellar mass concentration of $c = 7.12^{+1.53}_{-0.99}$ was estimated. A comparison with these measurements suggests that there is significant evolution in the stellar mass density distribution since $z \sim 1$. We compare the stellar mass density distributions between the two epochs on the same physical scale, showing that the stellar mass density in the cluster cores (R<0.2 Mpc) has to decrease since $z \sim 1$. We argue that this may be related to the build-up of the ICL+BCG component over cosmic time.

A build-up of stellar mass onto the outskirts (R>0.3 Mpc) is further required to match the observed stellar mass distribution in the descendant population. Given that the dark matter haloes in N-body simulations are also found to accrete matter onto the outer parts, a comparison between observations and simulation has the potential to constrain the stellar mass fraction of haloes that are being accreted by the clusters.

Acknowledgements

Based on observations made with the Isaac Newton Telescope through program IDs I10AN006, I10AP005, I10BN003, I10BP005, I11AN009, I11AP013. We thank Malin Velander, Emma Grocutt, Lars Koens and Catherine Heymans for help in acquiring the data. The Isaac Newton Telescope is operated on the island of La Palma by the Isaac Newton Group in the Spanish Observatorio del Roque de los Muchachos of the Instituto de Astrofísica de Canarias.

5.A Consistency checks

We compare the SMF of galaxies in the COSMOS field, as estimated using photometry in the *ugri*-bands, with the SMF of galaxies in the outermost areas of the cluster fields. Since the distance to the cluster centre is larger than the virial radius (or R_{200}), the cluster is expected to only be marginally over-dense compared to the field in that regime. Thus we use this comparison as a consistency check between the different surveys and filter sets.

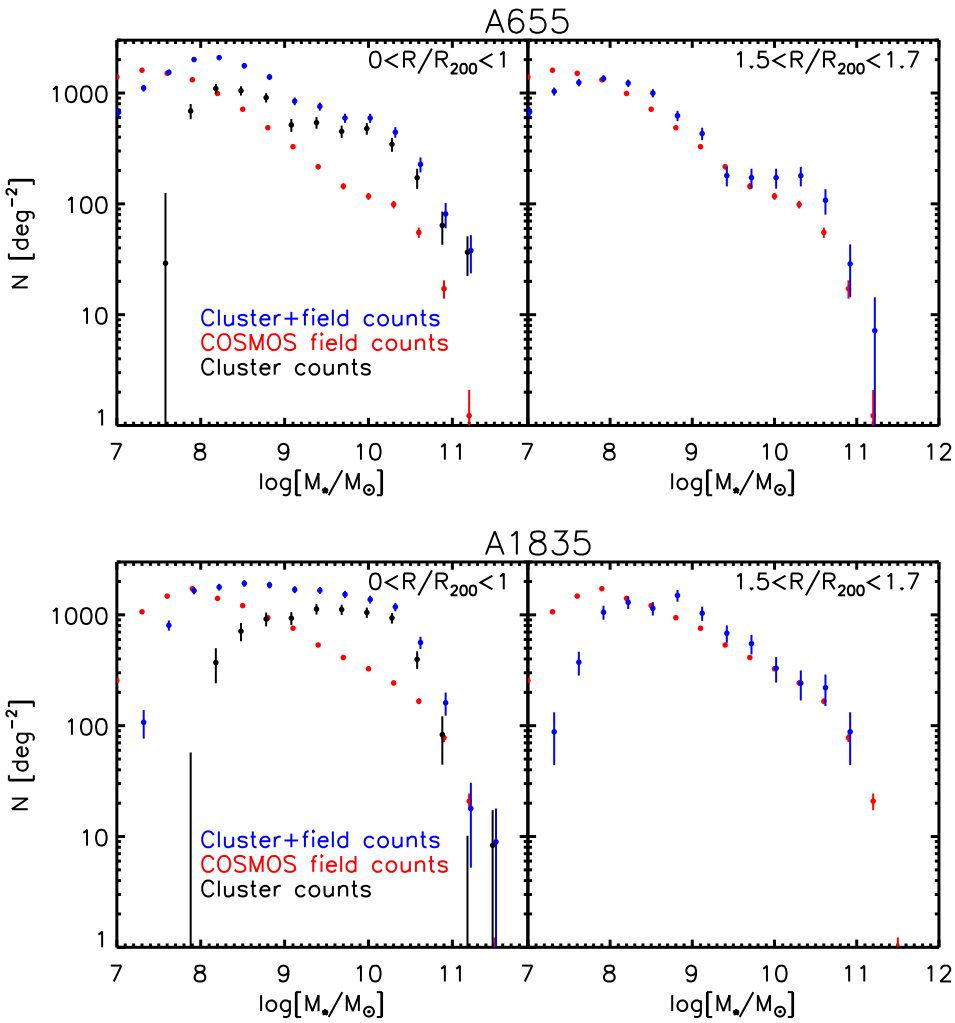

Figure 5.15: The SMF of A655 (*top*) and A1835 (*bottom*) in two radial bins. *Left*: The cluster inner part (R$<R_{200}$). *Right*: the outer part $1.5R_{200} < \mathrm{R} < 1.7R_{200}$. The expected background (field) counts from the COSMOS survey are indicated in red, and the black points are the background subtracted values. The outer radial bin shows only a mild over-density of counts compared to the field values.

We obtain the stellar masses from the SED-fitting code FAST, where we fix the redshift to the median redshift of the cluster. This is thus no proper field SMF, since all distance moduli are equal to the clusters'. However, upon subtracting the COSMOS field value from the cluster-field counts, we obtain the stellar mass function in this outer radial bin of the cluster. The photometric data of the COSMOS field is substantially ($\sim$ 1-2 mags) deeper than our cluster data, leading to a different stellar mass completeness limit (see the difference in the drop in galaxy counts at the low-mass end of the SMF for the different surveys). For the work presented in this paper, the incompleteness in that regime does not significantly affect the stellar mass distribution (nor the number density distribution for sources with stellar mass exceeding 10^9). For the measurement of the cluster galaxy stellar mass function in this cluster sample (van der Burg et al., in prep), we will perform a series of simulations to assess and correct for the stellar mass incompleteness at lower masses.

Bibliography

Ahn, C. P., Alexandroff, R., Allende Prieto, C., et al. 2013, ArXiv e-prints

Andreon, S. & Hurn, M. A. 2010, MNRAS, 404, 1922

Baldry, I. K., Balogh, M. L., Bower, R. G., et al. 2006, MNRAS, 373, 469

Bauer, A. H., Baltay, C., Ellman, N., et al. 2012, ApJ, 749, 56

Behroozi, P. S., Wechsler, R. H., & Conroy, C. 2013, ApJ, 770, 57

Bell, E. F. & de Jong, R. S. 2001, ApJ, 550, 212

Bell, E. F., McIntosh, D. H., Katz, N., & Weinberg, M. D. 2003, ApJS, 149, 289

Benson, A. J., Lacey, C. G., Baugh, C. M., Cole, S., & Frenk, C. S. 2002, MNRAS, 333, 156

Binney, J. & Tremaine, S. 2008, Galactic Dynamics: Second Edition (Princeton University Press)

Bower, R. G., Benson, A. J., Malbon, R., et al. 2006, MNRAS, 370, 645

Boylan-Kolchin, M., Bullock, J. S., & Kaplinghat, M. 2011, MNRAS, 415, L40

Brammer, G. B., van Dokkum, P. G., & Coppi, P. 2008, ApJ, 686, 1503

Budzynski, J. M., Koposov, S. E., McCarthy, I. G., McGee, S. L., & Belokurov, V. 2012, MNRAS, 423, 104

Bullock, J. S. 2010, ArXiv e-prints

Burke, C. & Collins, C. A. 2013, MNRAS, 434, 2856

Burke, C., Collins, C. A., Stott, J. P., & Hilton, M. 2012, MNRAS, 425, 2058

Carlberg, R. G., Yee, H. K. C., & Ellingson, E. 1997, ApJ, 478, 462

Cen, R. 2014, ApJ, 781, 38

Chabrier, G. 2003, PASP, 115, 763

Clowe, D., Markevitch, M., Bradač, M., et al. 2012, ApJ, 758, 128

Comerford, J. M. & Natarajan, P. 2007, MNRAS, 379, 190

Contini, E., De Lucia, G., Villalobos, A., & Borgani, S. 2013, ArXiv e-prints

Covey, K. R., Ivezić, Ž., Schlegel, D., et al. 2007, AJ, 134, 2398

Dalla Vecchia, C. & Schaye, J. 2008, MNRAS, 387, 1431

De Lucia, G. & Blaizot, J. 2007, MNRAS, 375, 2
Demarco, R., Wilson, G., Muzzin, A., et al. 2010, ApJ, 711, 1185
Diemer, B., More, S., & Kravtsov, A. V. 2013, ApJ, 766, 25
Dressler, A. 1980, ApJ, 236, 351
Duffy, A. R., Schaye, J., Kay, S. T., & Dalla Vecchia, C. 2008, MNRAS, 390, L64
Efstathiou, G. 2000, MNRAS, 317, 697
Evrard, A. E., Bialek, J., Busha, M., et al. 2008, ApJ, 672, 122
Fadda, D., Girardi, M., Giuricin, G., Mardirossian, F., & Mezzetti, M. 1996, ApJ, 473, 670
Ghigna, S., Moore, B., Governato, F., et al. 2000, ApJ, 544, 616
Gillis, B. R., Hudson, M. J., Erben, T., et al. 2013, MNRAS, 431, 1439
Giodini, S., Pierini, D., Finoguenov, A., et al. 2009, ApJ, 703, 982
Gladders, M. D. & Yee, H. K. C. 2000, AJ, 120, 2148
Gonzalez, A. H., Sivanandam, S., Zabludoff, A. I., & Zaritsky, D. 2013, ApJ, 778, 14
Guo, Q., White, S., Li, C., & Boylan-Kolchin, M. 2010, MNRAS, 404, 1111
Henriques, B. M. B., White, S. D. M., Lemson, G., et al. 2012, MNRAS, 421, 2904
High, F. W., Stubbs, C. W., Rest, A., Stalder, B., & Challis, P. 2009, AJ, 138, 110
Hoekstra, H., Donahue, M., Conselice, C. J., McNamara, B. R., & Voit, G. M. 2011, ApJ, 726, 48
Hogg, D. W. 1999, ArXiv Astrophysics e-prints
Ilbert, O., Salvato, M., Le Floc'h, E., et al. 2010, ApJ, 709, 644
Kauffmann, G., White, S. D. M., Heckman, T. M., et al. 2004, MNRAS, 353, 713
Klypin, A., Kravtsov, A. V., Valenzuela, O., & Prada, F. 1999, ApJ, 522, 82
Knobel, C., Lilly, S. J., Kovač, K., et al. 2013, ApJ, 769, 24
Kriek, M., van Dokkum, P. G., Labbé, I., et al. 2009, ApJ, 700, 221
Kuijken, K. 2008, A&A, 482, 1053
Lasker, B. M., Lattanzi, M. G., McLean, B. J., et al. 2008, AJ, 136, 735
Lidman, C., Iacobuta, G., Bauer, A. E., et al. 2013, MNRAS, 433, 825
Lidman, C., Suherli, J., Muzzin, A., et al. 2012, MNRAS, 427, 550
Lin, Y.-T. & Mohr, J. J. 2004, ApJ, 617, 879
Lin, Y.-T., Mohr, J. J., & Stanford, S. A. 2004, ApJ, 610, 745
Lin, Y.-T., Stanford, S. A., Eisenhardt, P. R. M., et al. 2012, ApJ, 745, L3
Magnier, E. A. & Cuillandre, J.-C. 2004, PASP, 116, 449
Mahdavi, A., Hoekstra, H., Babul, A., Balam, D. D., & Capak, P. L. 2007, ApJ, 668, 806
Mandelbaum, R., Seljak, U., & Hirata, C. M. 2008, J. Cosmology Astropart. Phys., 8, 6
Muzzin, A., Marchesini, D., Stefanon, M., et al. 2013a, ApJ, 777, 18
Muzzin, A., Marchesini, D., Stefanon, M., et al. 2013b, ApJS, 206, 8
Muzzin, A., Wilson, G., Lacy, M., Yee, H. K. C., & Stanford, S. A. 2008, ApJ,

686, 966
Muzzin, A., Wilson, G., Yee, H. K. C., et al. 2012, ApJ, 746, 188 (M12)
Muzzin, A., Wilson, G., Yee, H. K. C., et al. 2009, ApJ, 698, 1934
Muzzin, A., Yee, H. K. C., Hall, P. B., Ellingson, E., & Lin, H. 2007, ApJ, 659, 1106
Nagai, D. & Kravtsov, A. V. 2005, ApJ, 618, 557
Natarajan, P., Kneib, J.-P., & Smail, I. 2002, ApJ, 580, L11
Navarro, J. F., Frenk, C. S., & White, S. D. M. 1997, ApJ, 490, 493
Peng, Y.-j., Lilly, S. J., Kovač, K., et al. 2010, ApJ, 721, 193
Peng, Y.-j., Lilly, S. J., Renzini, A., & Carollo, M. 2012, ApJ, 757, 4
Pérez-González, P. G., Rieke, G. H., Villar, V., et al. 2008, ApJ, 675, 234
Rines, K., Geller, M. J., Diaferio, A., & Kurtz, M. J. 2013, ApJ, 767, 15
Sand, D. J., Graham, M. L., Bildfell, C., et al. 2011, ApJ, 729, 142
Schaye, J., Dalla Vecchia, C., Booth, C. M., et al. 2010, MNRAS, 402, 1536
Schlegel, D. J., Finkbeiner, D. P., & Davis, M. 1998, ApJ, 500, 525
Sereno, M. & Covone, G. 2013, MNRAS
Sifón, C., Menanteau, F., Hasselfield, M., et al. 2013, ApJ, 772, 25
Springel, V., White, S. D. M., Jenkins, A., et al. 2005, Nature, 435, 629
Tinker, J., Kravtsov, A. V., Klypin, A., et al. 2008, ApJ, 688, 709
van der Burg, R. F. J., Muzzin, A., Hoekstra, H., et al. 2013, A&A, 557, A15 (vdB13)
van der Burg, R. F. J., Muzzin, A., Hoekstra, H., et al. 2014, A&A, 561, A79 (vdB14)
van Dokkum, P. G. 2001, PASP, 113, 1420
Wechsler, R. H., Bullock, J. S., Primack, J. R., Kravtsov, A. V., & Dekel, A. 2002, ApJ, 568, 52
Weinmann, S. M., Pasquali, A., Oppenheimer, B. D., et al. 2012, ArXiv e-prints
Wilson, G., Muzzin, A., Yee, H. K. C., et al. 2009, ApJ, 698, 1943
Woo, J., Dekel, A., Faber, S. M., et al. 2013, MNRAS, 428, 3306
Yee, H. K. C., Ellingson, E., & Carlberg, R. G. 1996, ApJS, 102, 269
Zibetti, S., White, S. D. M., Schneider, D. P., & Brinkmann, J. 2005, MNRAS, 358, 949